1-15-2013

Boron-carbon-nitrogen foam surfaces for thermal physisorption applications

Rajib Paul
Birck Nanotechnology Center, Purdue University, paul24@purdue.edu

A. A. Voevodin
Birck Nanotechnology Center, Purdue University; US Air Force Research Laboratory, avoevodi@purdue.edu

J. J. Hu
US Air Force Research Laboratory

P. B. Amama
US Air Force Research Laboratory; University of Dayton

S. Ganguli
US Air Force Research Laboratory

See next page for additional authors

Authors
Rajib Paul, A. A. Voevodin, J. J. Hu, P. B. Amama, S. Ganguli, A. K. Roy, Dmitry Zemlyanov, and Timothy S. Fisher

Thin Solid Films 528 (2013) 187–193

Contents lists available at SciVerse ScienceDirect

Thin Solid Films

journal homepage: www.elsevier.com/locate/tsf

Boron–carbon–nitrogen foam surfaces for thermal physisorption applications

R. Paul [a,*], A.A. Voevodin [a,b], J.J. Hu [b], P.B. Amama [b,c], S. Ganguli [b], A.K. Roy [b], D. Zemlyanov [a], T.S. Fisher [a,b,*]

[a] Birck Nanotechnology Center, Purdue University, West Lafayette, IN 47907, United States
[b] Materials and Manufacturing Directorate, Air Force Research Laboratory, WPAFB, OH 45433, United States
[c] University of Dayton Research Institute, University of Dayton, Dayton, OH 45469, United States

ARTICLE INFO

Available online 6 November 2012

Keywords:
Porous carbon
Boron nitrogen doping
Desorption
Enthalpy
Thermal conductivity

ABSTRACT

A surface chemical treatment of highly porous carbon foams was adopted to synthesize boron–carbon–nitrogen (B–C–N) foams for thermal energy storage and release using an adsorption/desorption cycle with lightweight hydrocarbons. Microwave treatment in boric acid and urea was used to modify carbon foams with a B–C–N surface. Depending on the initial carbon foam state, B–C–N surface layers were produced with both amorphous and crystalline structures. The resultant B–C–N foams were characterized by TEM, XPS, XRD, FESEM and Raman measurements to quantify their stoichiometry, structure, and morphology. Adsorption enthalpy with methanol and thermal stability of foams was analyzed with DSC and TGA respectively. Thermal conductivity was measured by a transient laser flash technique. Results indicate that the crystalline graphitic carbon foam produces superior B–C–N surfaces compared to amorphous carbon foam. The crystalline B–C–N foams are found to provide the highest adsorption capacity, better thermal and oxidation stability.

1. Introduction

Increased attention to energy efficiency has spurred renewed interest in thermal storage, particularly associated with intermittent energy sources and waste heat recovery cycles [1]. Adsorption/desorption cycles with lightweight hydrocarbons are appealing for their simplicity in storing and releasing thermal energy [1]. For these cycles, a porous material with high thermal conductivity, thermal stability and excellent adsorption behavior for lightweight hydrocarbons is required [2].

Thermally conductive metal foams can offer advantages over traditional fin and extended-surface heat transfer structures, particularly those requiring low mass density due to weight or inertial considerations. However, the thermal performance of metal foams in common single-phase convection conditions is typically not superior to traditional finned heat exchangers [3,4]. For multiphase liquid–vapor flows, the parallel vapor escape routes offered by mesoporous foams can alleviate catastrophic thermal behavior in regular fin arrays caused by vapor backflow [2]. Among other porous materials, carbon foams, as a macroporous material, are known for superior thermal conductivity and light weight [5], but they suffer from inferior adsorption enthalpy and susceptibility to oxidation at temperatures above 550 °C.

Modification of carbon surfaces with boron and nitrogen to form B–C–N structures can enhance adsorption enthalpy as compared to pure carbon surfaces [6]. Further, the B–C–N surface morphology offers an advantage of oxidation stability [7]. The crystalline structure of B–C–N surfaces is expected to improve physisorption efficiency based on enhanced affinity of the adsorbate near local hexagonal B–N domains within the graphene structure [8]. Among other adsorbate–adsorbent pairs, such as zeolite–water [9–12], activated carbon–ammonia [13–15], silica gel–water [16,17], calcium chloride–carbon–ammonia [18–20] and other composite adsorbent–ammonia systems [21], activated carbon–methanol [22–25] has often being selected due to the high weight fraction of methanol adsorption. However the catalytic effect of activated carbon on methanol, and its poor thermal conductivity and thermal stability suggests that alternative adsorbents should be developed [26].

The physisorption performance (i.e., adsorption/desorption efficiency and cycle time) are strongly related to the thermal conductivity of the adsorbent and its surface chemistry [2]. Adsorption and desorption processes also depend strongly on surface crystallinity and morphology of the adsorbent. Systematic study of the influence of crystallinity and morphology on the physisorption properties of carbon foam and modified carbon foam would be of interest. Here, we use both amorphous and crystalline carbon foams as precursors for B–C–N foams by surface treatment. This work investigates microwave-assisted thermo-chemical modification of those carbon foams for surface synthesis of amorphous and crystalline B–C–N foam microstructures. These microstructures are characterized for their relative physisorption of methanol, thermal stability and thermal conductivity studies.

* Corresponding authors. Tel.: +1 765 494 5627; fax: +1 765 494 0539.
E-mail addresses: paul24@purdue.edu (R. Paul), tsfisher@purdue.edu (T.S. Fisher).

0040-6090/$ – see front matter © 2012 Elsevier B.V. All rights reserved.
http://dx.doi.org/10.1016/j.tsf.2012.08.059

2. Experimental details

Amorphous as well as crystalline graphitic carbon foams, KFOAM® (Manufacturer: Koppers Inc., Pittsburgh), of approximately 75% open porosity were incorporated with boron and nitrogen molecules through microwave heat-assisted chemical treatment. To clarify the distinction between amorphous and crystalline carbon foams, we note that the crystalline carbon foam was obtained by graphitization of amorphous carbon foam at extremely high temperature (2800 °C) by the manufacturer.

In the first step of modification, an aqueous solution of boric acid [$B(OH)_3$] and urea [$CO(NH_2)_2$] in 1:24 M proportion (0.5 g and 12 g respectively) was prepared. A 10 mL solution was taken in a vial together with carbon foam to treat with microwave heating (Biotage Initiator, NC, USA) at 20 bar pressure and 120 °C temperature using 400 W power (2.45 GHz) for 30 min to create a high thermal gradient across the foam surface and solution, causing molecules to diffuse into the carbon foam material. The amorphous carbon and graphitic carbon foams were treated separately in the microwave chamber, and the final foam materials were kept in a vacuum desiccator for at least 12 h to remove water molecules. The chemically treated foams were then annealed at 1100 °C in a tube furnace with constant N_2 gas flow for 18 h to promote a chemical reaction between the foam and chemicals as well as to remove unreacted chemicals and oxides.

Scanning electron microscope (SEM) images were taken from the carbon foam samples using a FEI-DB235 focused ion beam (FIB) microscope under its electron column. The FIB microscope was also equipped with an Omniprobe manipulator that was employed to prepare transmission electron microscope (TEM) specimens of the cross-sectional microstructure proceeding from the surface to the body. The FIB microscope was operated using 5 keV electron beams and 30 keV Ga^+ ion beams. To protect the foam surface structure from incident ion-beam bombardment, a surface Pt protection cap was deposited using a gas injection system (GIS). This was followed by Pt deposition of approximately 2 μm thickness using a moderately low ion current. The as-prepared TEM specimens were observed using a FEI Titan™ 80–300 S/TEM, which was equipped with a field emission gun and Cs-corrector for studying high resolution microstructures.

Chemical composition was investigated by X-ray photoelectron spectroscopy (XPS) using a Kratos Ultra DLD spectrometer with monochromatic Al·Kα radiation ($h\nu = 1486.58$ eV). Survey and high-resolution spectra were collected from a $700 \times 400\ \mu m^2$ spot size at normal incidence with respect to the sample surface using fixed analyzer pass energies of 160 and 20 eV for the survey and high-resolution spectra, respectively. XPS data were analyzed with commercially available CasaXPS software (www.casxps.com), and individual peaks were fitted with a Gaussian/Lorentzian (GL) function. A charge neutralizer was used for BCN foams due to their moderate electrical conductivity, and the resulting spectra were then corrected on the binding energy scale, using the C 1s peak position at 284.5 eV as a reference for graphitic carbon.

A Bruker D8 focused X-ray diffractometer was utilized to evaluate the crystalline nature of the carbon and B–C–N foams. A Cu·K(alpha) X-ray source, 3-circle goniometer and lynseye 1D detector were used to obtain diffraction data with 15 rpm rotation of the substrate holder keeping in mind the porous structure of the foams. A micro-Raman spectrometer equipped with a Senterra confocal Raman system (Bruker Optics Inc., Billerica, MA) and a 50× air objective at 633 nm laser excitation was used to collect Raman spectra of amorphous and graphitic carbon foams and their B–C–N counterparts. The laser power and accumulation time during measurements were 20 mW and 10 s.

The adsorption/desorption enthalpies of the carbon and B–C–N foams for methanol adsorption were evaluated using a differential scanning calorimeter (TA, Q100, V9.8). The foam materials were inserted into an edge-sealed aluminum pan with a top pinhole together with methanol. The measurements were taken under a ramped temperature process (−20 °C to 150 °C) at a rate of 20 °C/min with a constant nitrogen flow (50 ml/min). The pinhole on the pan surface minimized boiling-point drift caused by increased pressure inside the pan during the temperature ramp. The latent heat of evaporation of methanol and the desorption enthalpy of methanol with foams were evaluated through separate experiments involving (a) methanol only and (b) methanol with foam, keeping all other experimental parameters identical. The thermal stability of the foams was studied by thermo-gravimetric analysis (TGA) and derivative thermogravimetry (DTG) using a TA SDT 600 instrument under non-isothermal conditions from room temperature to 1000 °C. The measurements were performed under flowing dry air (100 sccm) using typically 15–20 mg of sample, heated in a ceramic crucible at 5 °C/min.

Thermal conductivity measurements were performed by a laser flash diffusion technique. In this technique, the open cells of the foams were filled with an epoxy resin, EPON 862/Epikure W by vacuum-assisted resin infusion and then cured at 177 °C for 3 h. Next, the specimens were grinded and polished into 10 mm × 10 mm × 2 mm pieces. In order to prevent the laser beam from transmitting directly through the specimen to the detector, a 200 nm Au layer was sputter-coated on either side of the specimens. Finally, in order to achieve uniform emissivity and uniform absorption of the laser beam, a thin graphite layer was spray-coated on the specimens per ASTM E1461-07.

3. Results and discussion

The high thermal gradient across the foam and solution surfaces created during the microwave heating helped the reactant molecules to diffuse into the carbon foam materials. These properties of the B–C–N foams produced are dependent on this diffusion process. The properties of B–C–N foams obtained from amorphous and crystalline carbon foams are evaluated to determine if the diffusion process is dependent on the crystallinity of the carbon foams.

Fig. 1 shows SEM images of amorphous and crystalline B–C–N foam surfaces. Smooth, crack-free foam surfaces are evident in Fig. 1(a) and (b) for amorphous B–C–N. Conversely, the crystalline foam surfaces (Fig. 1(c) and (d)) are rough and consist of crystalline ligaments separated by cracks. The cracks are the result of high-temperature annealing (2800 °C) during the crystalline graphitic foam manufacturing procedure. Presence of these cracks essentially alters the porosity of crystalline carbon foam from macroporous to microporous. These cracks could assist boron and nitrogen diffusion during the chemical modification process to make B–C–N foams. Consequently, a stoichiometric analysis to differentiate between the boron and nitrogen content in the B–C–N foams obtained from chemical treatment of crack-less amorphous and multi-cracked crystalline graphitic carbon foams was performed by XPS measurements.

Fig. 2 compares survey XPS spectra obtained from B–C–N foams by microwave-assisted thermochemical surface treatment of amorphous and crystalline carbon foams. The comparison clearly shows that foams obtained from crystalline carbon foams have a larger content of nitrogen and boron. Estimates of the foam surface's elemental composition reveal that the surface of crystalline B–C–N foams contains approximately 15 at.% B, 14 at.% N, and 5 at.% O, with carbon as the remainder. At the same time the surface of amorphous B–C–N foam contains approximately 7 at.% B, 5 at.%N, and 12 at.% O. The variation of the B–C–N foams' chemical composition was within 1–2 at.% for repeated samples treated under identical condition.

Detailed high-resolution scans of B *1s* and N *1s* regions reveal several possible binding configurations of boron and nitrogen atoms in the B–C–N structure. Fig. 3(a) and (b) provides examples of N *1s* and B *1s* XPS spectra for amorphous and crystalline carbon foams respectively. The B *1s* spectra were fit with three peaks corresponding to boron in boron oxide, boron nitride, and boron carbide, respectively [27–29]. The N *1s* spectra were also fit with peaks corresponding to

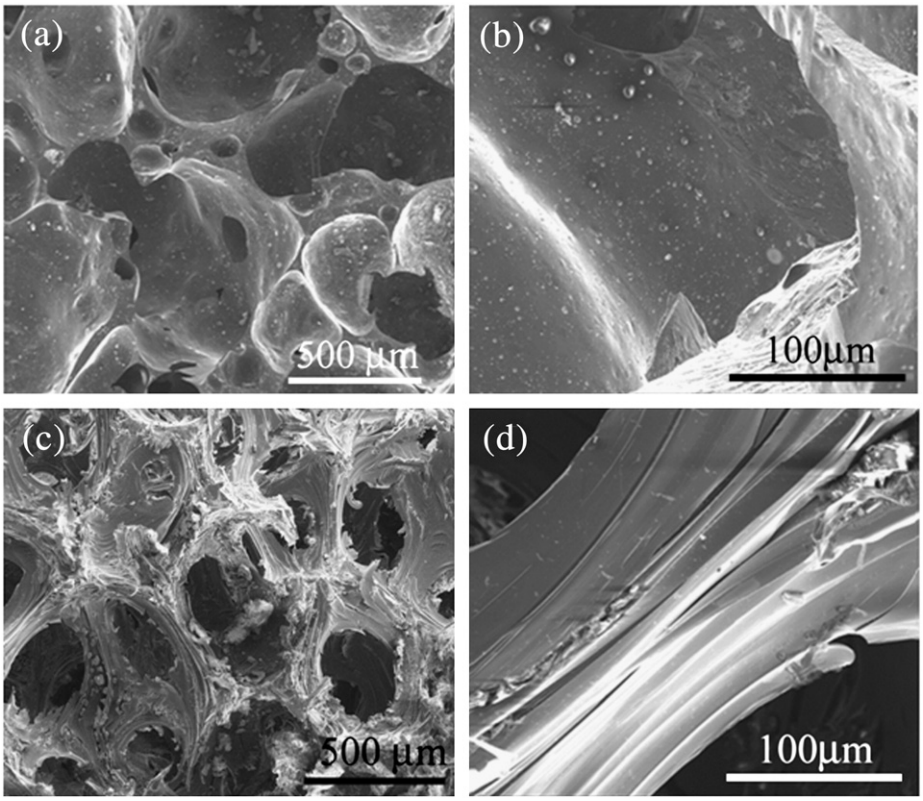

Fig. 1. SEM images (a, b) taken from amorphous B–C–N foam, and (c, d) taken from crystalline B–C–N foam.

nitrogen bonding with carbon in pyridine-like bonds ($-NC_2$, where a N atom is bonded with two neighboring carbon atoms and has a free electron creating a defect site), graphite-like or carbon substitutional bonds (NC_3, where a N atom substitutes a C atom in a hexagonal carbon ring and binds to three neighboring C atoms), and in boron nitride bonds, respectively [27,29,30]. Further details of the peak assignments in the B–C–N spectra can be found in a recent publication [31].

Fig. 3 indicates clearly that crystalline foams have larger fractions of bonds in B – C and B – N configurations as compared to amorphous B–C–N foams. This observation was confirmed by quantitative peak area analysis to estimate percentages of boron and nitrogen bonded as B – O, B – C, and B – N. The results are presented in Table 1. Crystalline B–C–N foams have up to 5–6 at.% of boron and nitrogen in the B–N configuration. Interestingly, crystalline foams also have up to 6 at.% boron in B – C bonds. Crystalline foams also have a higher percentage of B – O bonds, as compared to amorphous B–C–N foams, even as the overall oxygen content in crystalline foams was approximately 5 at.% (half of the amount in the amorphous foam).

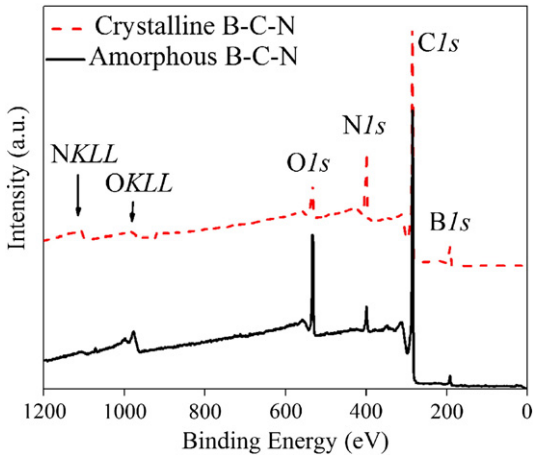

Fig. 2. XPS spectra of B–C–N foams obtained from amorphous and crystalline carbon foams by the microwave-assisted thermo-chemical treatment.

Notably, the percentage of nitrogen in B–N closely follows that of boron for crystalline foams, yielding a nearly one-to-one ratio as observed in prior work [31]. This observation indicates formation of B–N domains as opposite to random substitution of carbon with boron and nitrogen atoms, following the conversion of carbon foam surfaces to B–C–N. Nitrogen is also engaged in carbon domains by direct substitution of carbon atoms in a graphitic configuration, or in pyridine-like bonding arrangements. Thus, the resulting B–C–N foam surface consists predominantly of distinct B–N and carbon domains, with evidence of B – C bonds. Both of these domains contain defects as evidenced by high relative percentages of nitrogen pyridine bonding and boron oxide. Oxygen detected by XPS is most likely an impurity. On the foam surface, the TEM observation showed that boron oxide segregates and therefore oxygen is not included in carbon–boron–nitrogen network. The binding energy of O 1s peak is 532.5 eV, which is very close diboron(III) trioxide [32]. The boron oxide contaminations stay mainly on the foam surface; whereas at the annealing temperature above 900 °C the B and N atoms (B–N domains) propagate deeper into the carbon bulk to substitute C atoms [31] implying surface depletion of B–N. The B–N surface depletion is much more prevalent for crystalline B–C–N foam due to the presence of microporous cracks as compared to amorphous B–C–N foam. This fact has been reflected in the B 1s spectra of Fig. 3, where the fraction B – N bonds seem to be higher for crystalline B–C–N foam than the amorphous one. XPS is a surface characterization technique with the information depth of 5–10 nm, therefore the spectra in Fig. 3 represent only the surface stochiometry on the material. The intensities in Fig. 3 are in arbitrary units and they were normalized for better visualization.

The X-ray diffraction spectra of amorphous carbon foam and the B–C–N obtained from this foam are shown in Fig. 4(a). The presence of broad hump at lower angle (~12°) along with broad (002)

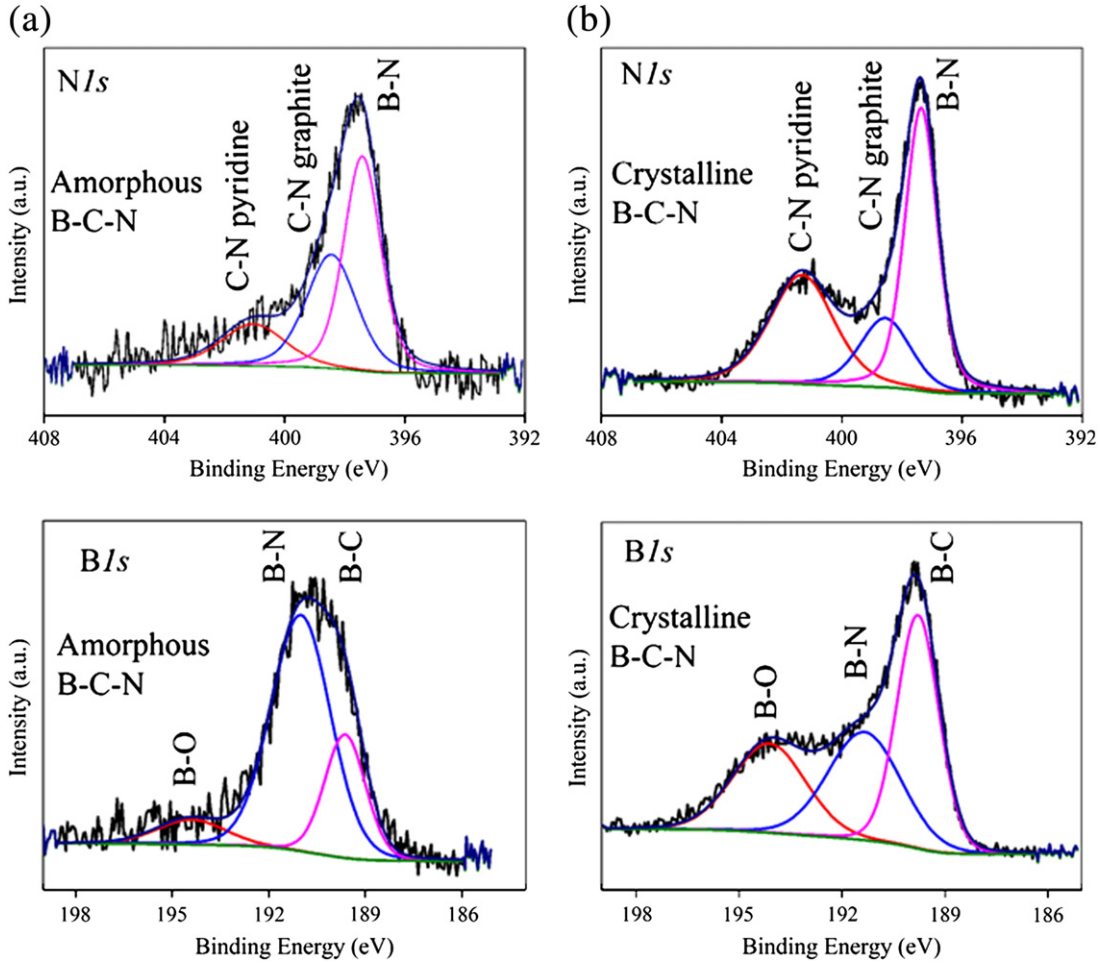

Fig. 3. Detailed XPS spectra of N 1s and B 1s regions for (a) amorphous and (b) crystalline B–C–N foams.

peak at ~26° and (100) peak at ~43° indicates amorphous nature of the carbon foam, while an onset of crystallinity is suggested in Fig. 4(a) for the B–C–N foams. This onset in crystallinity for B–C–N foam could be correlated with the annealing process at 1100 °C for 18 h. Nevertheless, there were no sharp diffraction peaks for these B–C–N foams, and they are considered to be predominantly amorphous. The high-temperature, long-duration annealing process not only helps in the removal of unreacted chemicals but also promotes some crystallization at the surface of this B–C–N foam. The X-ray spectrum for the crystalline graphitic carbon foam (Fig. 4b) indicates intense diffraction peaks, such as (002), (101), (004), (103) and (110) at ~26.5, 44, 54.4, 59.2 and 77.1° respectively, and the crystallinity was found to persist after incorporating boron and nitrogen. B–C–N materials have been found to form a solid solution between B–N and carbon domains due to the strong ionic attraction between B and N ions [33]. The interface regions between these domains are dominated with charged states due to sharing of charge between B–N and C regions. Such domain interfaces have zigzag edges with magnetically polarized edge states, which are coupled anti-ferromagnetically with those of nearby edges of similar character

Table 1
Boron and nitrogen content distribution of boron engaged in B–O, B–N, and B–C bonds, and nitrogen engaged in N–C pyridine-like, C–N graphite-like, and B–N bonding for the foams obtained from amorphous and crystalline carbon foams.

Foam type	B in B–O (at.%)	B in B–N (at.%)	B in B–C (at.%)	N in C–N pyridine (at.%)	N in C–N graphite (at.%)	N in B–N (at.%)	Foam stoichiometric formula
Amorphous	1	4	2	1	2	2	$B_{1.4}C_{14}N_1$
Crystalline	4	5	6	5	3	6	$B_{1.1}C_{4.7}N_1$

[34]. The magnetic properties of B–C–N materials are also reported to be superior to those of pure graphene or graphitic materials [34].

Micro-Raman spectra of amorphous carbon and BCN foams are shown in Fig. 5(a). The spectra are representative of amorphous glassy carbon with two dominant peaks: a D peak at 1332 cm^{-1} and a G peak at 1589 cm^{-1}. Fig. 5(b) shows the micro-Raman spectra obtained from graphitic foam and its B–C–N counterpart. These types of Raman spectra (Fig. 5b) identify the highly crystalline graphitic nature of the materials with D (1331 cm^{-1}), G (1580 cm^{-1}) and 2D (2684 cm^{-1}) peaks [31]. A weak shoulder (the D'band) at 1620 cm^{-1} for the B–C–N foam (Fig. 5b) indicates a higher density of defect states. The Raman spectrum is a characterizing signature for carbon-based materials, and the intensity ratio of D and G peaks (I_D/I_G) is a measure of the defect sites in graphitic materials [35]. The I_D/I_G ratio for amorphous carbon foam was ~1.15 while it increased to 1.22 for the B–C–N foam obtained from amorphous carbon foam. This implies an increment in defect density in the amorphous B–C–N foams. Conversely, the I_D/I_G ratio of graphitic carbon foam was 0.14 and was not found to change significantly upon B–C–N modification.

Fig. 6(a) contains a high-resolution TEM image taken from the amorphous B–C–N foam in cross section near the foam surface. The carbon foam itself is of amorphous phase. However, some crystalline fringes exist especially near the surface of the foam, as shown in Fig. 6(a), while crystallization inside the foam is absent. Fig. 6(b) shows the highly crystalline nature of the B–C–N foam. The lattice spacing was measured to approximately 0.34 nm, which corresponds to (002) planes. This lattice spacing indicates a B–C–N hybrid structure formed near the foam surface [36]. The crystal growth on surface likely results from the annealing process of the B–C–N foams at 1100 °C for

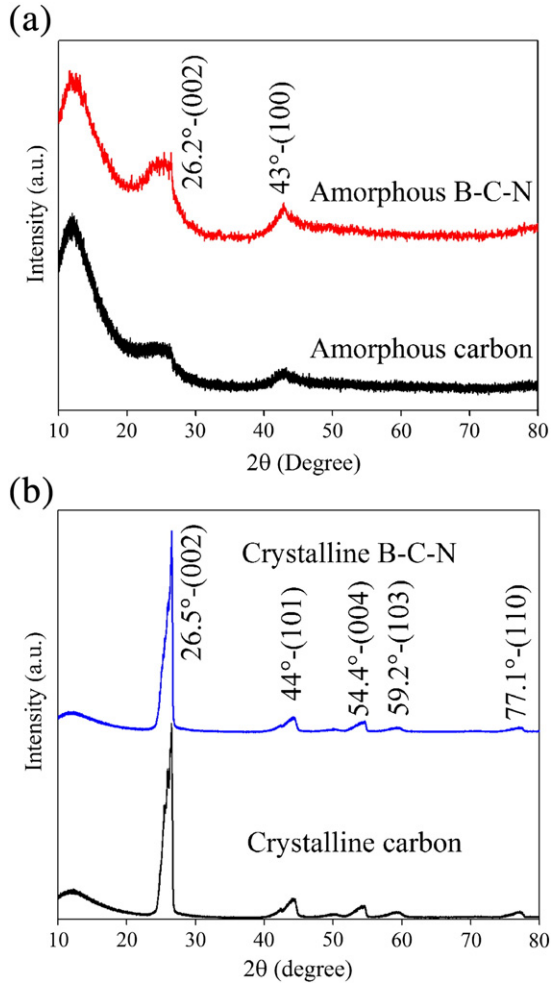

Fig. 4. X-ray diffraction spectra of (a) amorphous carbon and B–C–N foams and (b) crystalline graphite carbon and B–C–N foams.

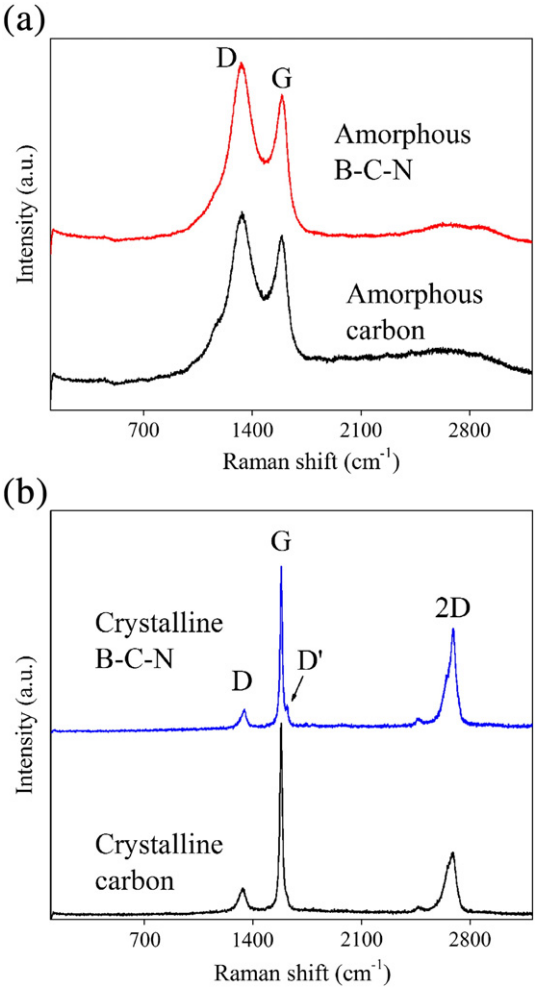

Fig. 5. Raman spectra of (a) amorphous carbon and B–C–N foams and (b) crystalline graphite carbon and B–C–N foams.

18 h. These TEM observations are in good agreement with the previously discussed XRD and Raman measurements.

The measured methanol desorption heat flow for pure amorphous and crystalline carbon foams and the modified B–C–N foams is shown in Fig. 7. The enthalpy of methanol-only evaporation was calculated from separate control experiments. The desorption enthalpies of foam samples were calculated by subtracting the control results. The heat flow through the amorphous B–C–N foam was found to improve a bit compared to that of amorphous carbon foam as shown in Fig. 7(a). A desorption shoulder of methanol for the amorphous B–C–N foam shifted towards higher temperature (Fig. 7a) compared to amorphous foam. The corresponding desorption enthalpies were 322 mJ/mg and 390 mJ/mg for amorphous carbon foam at its B–C–N counterpart, indicating a small but measureable increase.

For the crystalline B–C–N foam (Fig. 7(b)), a desorption shoulder exists near 85 °C that is not present for graphitic carbon foam. This feature produces a substantially increased desorption enthalpy from 500 to 870 mJ/mg upon B–C–N modification. This change in desorption enthalpy could be due to the higher defect density and charge sharing of boron and nitrogen atoms with carbon atoms on the B–C–N foam surface. Further, the crystalline foams are clearly superior to amorphous foams with respect to methanol desorption enthalpy. This characteristic is due to the inherently higher adsorption affinity of methanol to a graphene-type lattice [37]. Additionally, the effect of B–C–N modification appears to increase the enthalpy in rough proportion to the levels of boron and nitrogen incorporation, as indicated from the XPS results.

The oxidation behavior of the foams was studied using TGA in air. The TGA and corresponding DTG profiles for the foams in the as-received and modified B–C–N states are presented in Fig. 8(a) and (b) for amorphous and crystalline foams, respectively. The thermal stability of amorphous carbon foam is unchanged even after modification to B–C–N foam, while the crystalline foam shows improved thermal stability after modification to B–C–N. The crystalline carbon foam starts degradation at 570–580 °C while its modified B–C–N version shows robust stability up to 780 °C. This result implies improved thermal stability compared to that observed for few-layer B–C–N by Raidongia et al. [4], who reported degradation of B–C–N layers below 600 °C.

The bulk thermal properties of the foams were measured with a Netzsch LFA 457 laser flash thermal diffusivity system. The laser flash technique (or heat pulse) allows the measurement of the thermal diffusivity (α) of solid materials. It consists of applying a short duration (<1 ms) heat pulse to one face of a parallel sided sample and monitoring the temperature rise on the opposite face as a function of time. This temperature rise is measured with an infrared detector. Thermal diffusivity (α) can then be calculated using:

$$\alpha = \frac{\varpi\, d^2}{\pi\, t_{1/2}} \tag{1}$$

where, ϖ is a constant, d is the thickness of the specimen, and $t_{1/2}$ is the time for the rear surface temperature to reach half its maximum value. Sample weight and dimensions of the samples were precisely measured to calculate the density using a simple ratio of measured

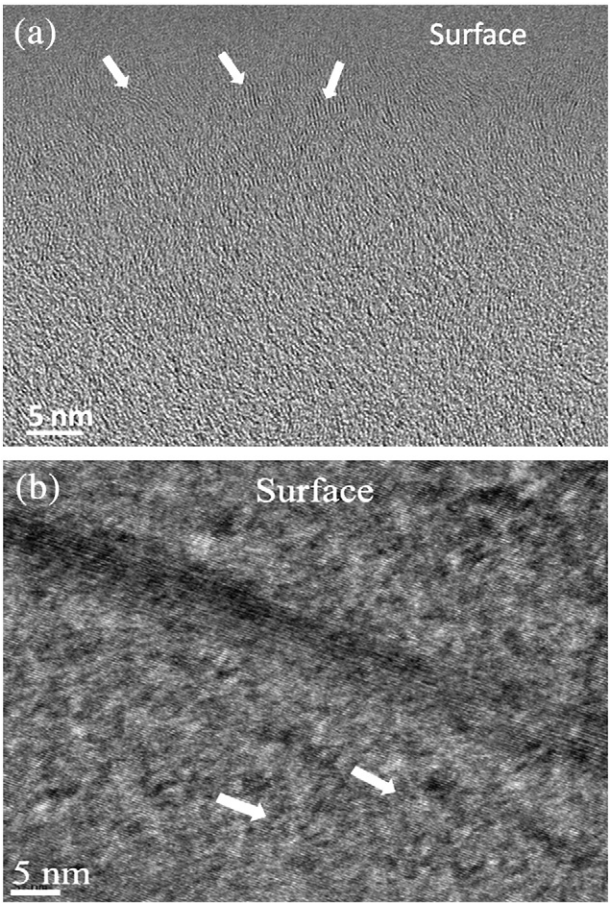

Fig. 6. High-resolution cross-sectional TEM images taken from (a) amorphous and (b) crystalline B–C–N foams. Arrows show the crystallinity near the surface.

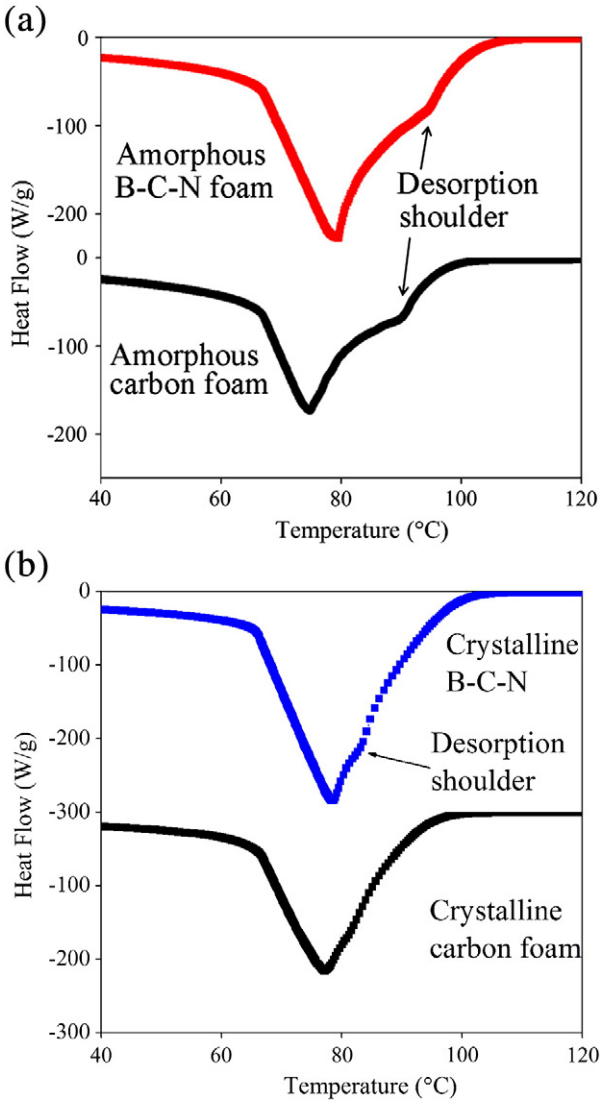

Fig. 7. DSC scans for (a) amorphous carbon and B–C–N foams, and (b) crystalline carbon and B–C–N foams.

weight to volume. Finally, using the heat capacity (C_p), measured using a TA Instruments modulated DSC Q5000 instrument, the density (ρ), thermal diffusivity (α), and thermal conductivity (k) of the samples were obtained at 24 °C from:

$$k = C_p \rho \alpha. \quad (2)$$

The laser flash thermal diffusivity measurements were performed following the ASTM E1461-07 guidelines. The calculated thermal conductivities of the specimens are presented in Fig. 9.

The thermal conductivity of the crystalline carbon foam increases by 135% on transformation to the B–C–N foam. This increase in thermal conductivity may be attributed to increased crystallinity. A modest increase of 30% in thermal conductivity is also noted for the amorphous carbon foams. The difference in the enhancements in thermal conductivities of the different foams may be due to the different degree of graphitization of the foams. Higher degree of graphitization leads to higher crystallinity, and therefore higher thermal conductivity. We note also that the thermal conductivity of graphitic carbon foams depends strongly on the density of that foam as observed by Alam et al. [5] and Klett et al. [38], who reported thermal conductivities of 150 W/(m-K) for a crystalline graphitic foam of density 0.6 g/cm^3, and only 42 W/m-K for a density of 0.26 g/cm^3. The density of graphitic foam used in our experiment is 0.23 g/cm^3. Hence, a thermal conductivity of 8 W/(m-K) as obtained in this experiment is reasonable. We also mention that the specific surface area for this type of crystalline carbon foam is 20000 m^2/m^3 with a density of 0.25–0.6 g/cm^3 and 75% porosity [31]. After chemical modification on the surface, the density (0.24 g/cm^3) of crystalline was found to remain approximately the same as before microwave treatment (0.23 g/cm^3) indicating the availability of the surface area on the B–C–N foam. However the density of amorphous carbon foam (0.37 g/cm^3) was found to decrease a bit for amorphous B–C–N foam (0.33 g/cm^3). This decrease might be due to the removal of some volatile amorphous constituents of the amorphous carbon foam during the annealing process of B–C–N foam preparation at 1100 °C.

4. Conclusion

This study has demonstrated microwave-assisted thermochemical treatment as an efficient method of synthesizing of both amorphous and crystalline B–C–N foams, from corresponding amorphous and crystalline carbon foam precursors. It further demonstrated that the surface of the carbon foams undergoes both chemical and structural changes. Boron and nitrogen surface incorporation is much more prevalent for crystalline carbon foams. The major results of the paper indicate that all tested thermal characteristics of the crystalline foam are strongly enhanced upon B–C–N modification: (i) increased methanol desorption enthalpy, (ii) enhanced thermal stability, and (iii) increased thermal conductivity. These three improvements suggest that the resultant foams may exhibit superior performance in thermal cycles that exploit physisorption for heat pumping and thermal storage.

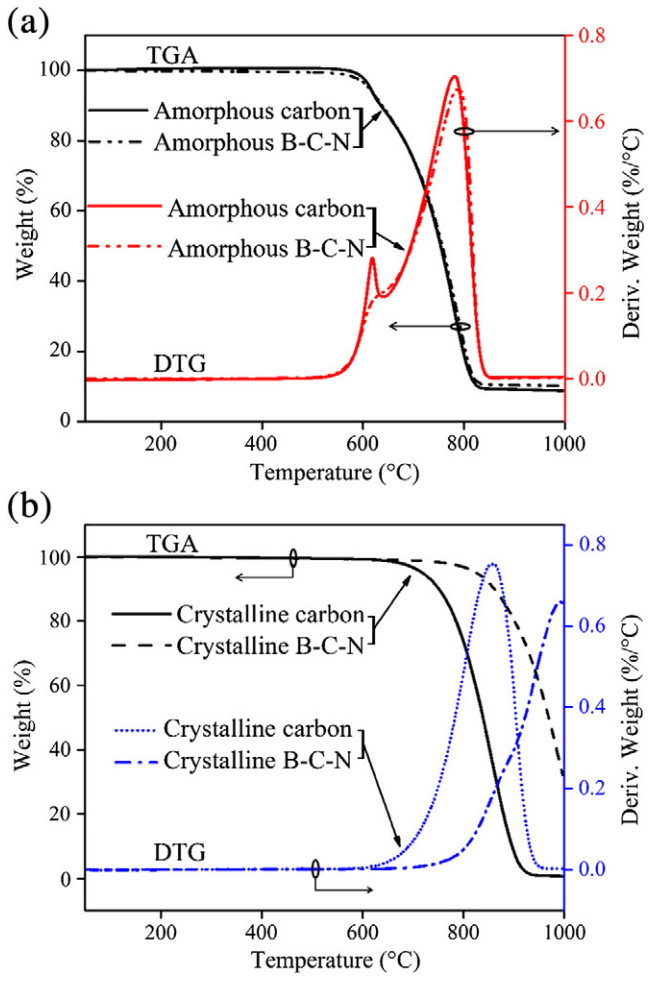

Fig. 8. (a) TGA and DTG profiles of amorphous carbon and B–C–N foams and (b) TGA and DTG profiles of crystalline carbon and B–C–N foams.

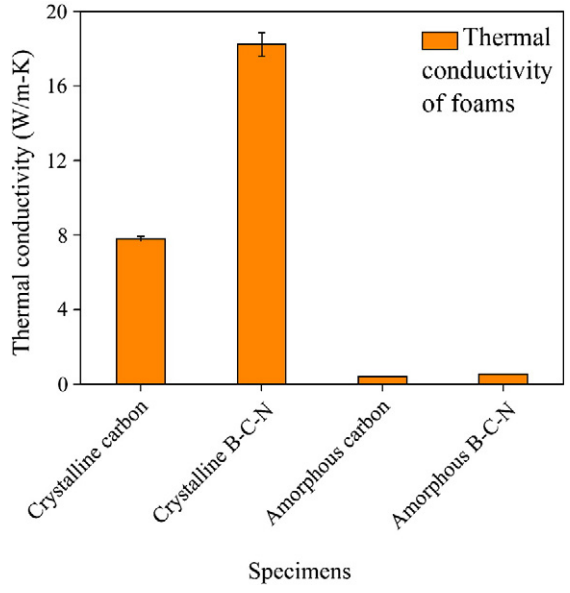

Fig. 9. Thermal conductivity of amorphous and crystalline carbon as well as B–C–N foams.

Acknowledgments

The authors are thankful to the U.S. Air Force Research Laboratory (AFRL), and its Office of Scientific Research (AFOSR, FA9550-12-1-0037) under the MURI program on Nanofabrication of Tunable 3D Nanotube Architectures (PM: Dr. Joycelyn Harrison), for financial support of this work. Thanks are due to Prof. Pipes and C. R. Misiego of Chemical Engineering, Purdue University, for their help in the DSC and TGA study. We are thankful to Purdue's Birck Nanotechnology Center staff for their assistance and cooperation.

References

[1] J. Deng, R.Z. Wang, G.Y. Han, Prog. Energ. Comb. Sci. 37 (2011) 172.
[2] W. Qu, I. Mudawar, Int. J. Heat Mass Transfer. 47 (2004) 2045.
[3] V.V. Calmidi, R.L. Mahajan, J. Heat Transfer 122 (2000) 559.
[4] A. Dąbrowski, Adv. Colloid Interface Sci. 93 (2001) 135.
[5] M.K. Alam, B. Maruyama, Exp. Heat Transfer 17 (2004) 227.
[6] K. Raidongia, A. Nag, K.P.S.S. Hembram, U.V. Waghmare, R. Datta, C.N.R. Rao, Chem. Eur. J. 16 (2010) 149.
[7] K. Raidongia, K.P.S.S. Hembram, U.V. Waghmare, M. Eswaramoorthy, C.N.R. Rao, Z. Anorg. Allg. Chem. 636 (2010) 30.
[8] N. Kumar, K.S. Subrahmanyam, P. Chaturbedy, K. Raidongia, A. Govindaraj, K.P.S.S. Hembram, A.K. Mishra, U.V. Waghmare, C.N.R. Rao, ChemSusChem 4 (2011) 1662.
[9] F. Poyelle, J.J. Guilleminot, F. Meunier, Ind. Eng. Chem. Res. 38 (1999) 298.
[10] M. Pons, S. Szarzynski, Int. J. Refrig. 23 (2000) 284.
[11] M. Tatlıer, A.E. Senatalar, Appl. Therm. Eng. 24 (2004) 69.
[12] M.D. Gross, B. Dawoud, in: Proceedings of the international sorption heat pump conference, Denver, USA, 2005.
[13] M.A. Lambert, Appl. Therm. Eng. 27 (2007) 1612.
[14] J.S. Metcalf, in: Proceedings of the international sorption heat pump conference, Denver, USA, 2005.
[15] A. Elgowainy, S. Shelton, J. Hogan, in: Proceedings of the international sorption heat pump conference, Denver, USA, 2005.
[16] Y. Hamamoto, K.C.A. Alam, A. Akisawa, T. Kashiwagi, Int. J. Refrig. 28 (2005) 344.
[17] H.M. Henning, E. Wiemken, in: Proceedings of ISES Solar World Congress. Gothenburg, Sweden, 2003.
[18] N.R. Thorpe, E.R. Critoph, Y. Zhong, in: Proceedings of the international sorption heat pump conference, Denver, USA, 2005.
[19] K. Wang, J.Y. Wu, Z.Z. Xia, S.L. Li, R.Z. Wang, Renewable Energy 33 (2008) 780.
[20] O.C. Iloeje, A.N. Ndili, S.O. Enibe, Energy 20 (1995) 1141.
[21] G. Cacciola, G. Restuccia, L. Mercadante, Carbon 33 (1995) 1205.
[22] R.Z. Wang, J.P. Jia, Y.H. Zhu, Y. Teng, J.Y. Wu, J. Cheng, Q.B. Wang, J. Sol. Energy Eng. 119 (1997) 214.
[23] G. Restuccia, G. Cacciola, Int. J. Refrig. 22 (1999) 18.
[24] F. Meunier, N. Douss, ASHRAE Trans. 2 (1990) 267.
[25] J.E.J. Hu, Sol. Energy 62 (1998) 325.
[26] D.C. Wang, Y.H. Li, D. Li, Y.Z. Xia, J.P. Zhang, Renewable Sustainable Energy Rev. 14 (2010) 344.
[27] A.R. Burke, C.R. Brown, W.C. Bowling, J.E. Glaub, D. Kapsch, C.M. Love, R.B. Whitaker, W.E. Moddeman, Surf. Interface Anal. 11 (1988) 353.
[28] R. Trehan, Y. Lifshitz, J.W. Rabalais, J. Vac. Sci. Technol. A 8 (1990) 4026.
[29] S.Y. Kim, J. Park, H.C. Choi, J.P. Ahn, J.Q. Hou, H.S. Kang, J. Am. Chem. Soc. 129 (2007) 1705.
[30] A.A. Voevodin, J.G. Jones, J.S. Zabinski, Zs. Czigány, L. Hultman, J. Appl. Phys. 92 (2002) 4980.
[31] R. Paul, A.A. Voevodin, D. Zemlyanov, A.K. Roy, T.S. Fisher, Adv. Func. Mater. 22 (2012) 3682.
[32] V.I. Nefedov, D. Gati, B.F. Dzhurinskii, N.P. Sergushin, Y.V. Salyn, Zh. Neorg. Khim. 20 (1975) 2307.
[33] W.Q. Han, H.G. Yu, Z. Liu, Appl. Phys. Lett. 98 (2011) 203112.
[34] Y.W. Son, M.L. Cohen, S.G. Louie, Nature 444 (2006) 347.
[35] R. Paul, S.N. Das, S. Dalui, R.N. Gayen, R.K. Roy, R. Bhar, A.K. Pal, J. Phys. D: Appl. Phys. 41 (2008) 055309.
[36] F. Zhuge, Z.G. Ji, H.P. He, Z.Z. Ye, L.P. Zhu, J. Cryst. Growth 310 (2008) 3869.
[37] Z.R. Tang, Physica B 405 (2010) 770.
[38] J. Klett, R. Hardy, E. Romine, C. Walls, T. Burchell, Carbon 38 (2000) 953.